IEEE INSTRUMENTATION & MEASUREMENT SOCIETY

Received 19 September 2023; revised 29 October 2023; accepted 31 October 2023. Date of publication 29 November 2023; date of current version 22 January 2024. The review of this paper was arranged by Associate Editor Katelyn Brinker.

*Digital Object Identifier 10.1109/OJIM.2023.3335537*

# Nondestructive Diagnostic Measurement Methods for HF RFID Devices With AI Assistance

**THIBAUT DELERUYELLE [1,2] (Member, IEEE), AMAURY AUGUSTE [1], FLORIAN SANANES [1], AND GHISLAIN OUDINET [1]**

[1]R&D Department, Yncréa Méditerranée, 83000 Toulon, France

[2]RFID-OC Team of the ACSE Department, IM2NP UMR 7334, 83000 Toulon, France

CORRESPONDING AUTHOR: T. DELERUYELLE (e-mail: thibaut.deleruyelle@yncrea.fr)

**ABSTRACT** This article presents different methods for noninvasive validation and diagnostics of contactless devices. The radio frequency systems studied here operate at 13.56 MHz. When manufacturing these systems in volume, it is essential to separate the fully functional devices from the totally defective ones or even from those communicating but have anomalies that will lead to a significant reduction of their lifetime. This article compares two noninvasive methods, one based on impedance measurements and the other on impulse response measurements. The advantages and drawbacks of these methods are presented and compared to their use in large-scale manufacturing. In addition to the proposed methods, this article describes two decision-making methodologies based on machine learning. This article compares also both measurement methods and machine learning tools. A robustness study shows the limitations of the employed techniques

**INDEX TERMS** Density-based spatial clustering of applications with noise (DBSCAN), impedance measurement, impulse response, machine learning, near-field communication (NFC), neural network, nondestructive, radio frequency identification (RFID).

## I. INTRODUCTION

CONTACTLESS devices operating in the near field at a frequency of 13.56-MHz play an important role in our daily lives. They fulfill different missions, such as payment (EMVCo: Europay Mastercard Visa Consortium) [1], identity (ICAO: International Civil Aviation Organization), transport (FeliCa: felicity card), access control, security (ISO 14443 [2], 15693 [3], NFC Forum (NFC: near-field communication [4]), etc.

These devices have to comply with many standards [5], [6], have different profiles (size, dimensions, and use), and have different lifespans.

Some travel tickets can have a life span of a few hours, bank cards have to work for about a couple of years, and passports have to work for more than eight years.

These devices must be manufactured at the lowest possible cost, and in order to control the cost, they are manufactured at high production rates. One of the key points in the manufacturing process is the attachment of the contactless chip to the antenna support, during this stage and despite the reliability of the machines, there is a tolerance in the positioning of the chip on the antenna as well as the pressure exerted on it. Some devices break, others are fully functional, and finally, some are weakened, which will lead to premature aging of the device or to malfunctions.

It is essential during the manufacturing process (e.g., passports) to isolate nonfunctional devices and remove them from circulation as soon as possible. Broken devices are the easiest to identify, while functional but damaged devices are more difficult to identify. It is essential that such identification can be done within the manufacturing cost constraints of these contactless devices. To achieve this, it must not significantly slow down the devices production flow.

Several studies focus on the characterization of radio frequency identification (RFID) chips, in operating mode [7] or not [8]. Several methods are capable of measuring the characteristics of assembled RFID devices. Some of them

are contact methods and require to put pins on the device as it is exposed in [9]. These methods, even if they offer good results, suffer from implementation difficulties and are incompatible with production capacities.

Noninvasive measurement methods offer several advantages. They do not require physical contact with the device under test, thus limiting possible electrostatic discharge problems. They can also be performed in the continuity of a production flow without interrupting it.

First, this article presents two methods of measurement that can meet these constraints, thereafter this article presents two AI-assisted computer decision-making methods for distinguishing between suitable and unsuitable products, with the added advantage of being able to achieve the decision task in real time, during the manufacturing personalization process. The first one is based on the study of the resonance of noncontact devices and allows to evaluate the characteristics of the devices through the study of their quality factor and resonance frequency, in the continuity of the work exposed in [10].

The second method is based on the impedance calculations by extracting the $S$ parameters in the contactless environment as presented by [11] and [12].

For the purposes of the study, about a hundred representative devices were studied and divided into three categories, fully functional devices are classified in the "OK" family, and broken devices in the "KO" family. The last family includes devices that can be personalized but have a reduced lifespan, this family is the Nearly Broken "NB" family. These three populations of samples were created after quality studies on functional, defective, and semi-defective samples. The problematic samples were analyzed by X-ray or acoustic microscopy.

The work presented in this article shows the advantages and disadvantages of these two measurement methods in characterizing the reliability of contactless devices in a manufacturing and customization context.

Following the description of the measurement methods, solutions allowing automatic rejections of damaged devices are considered. Several studies [13], [14], [15], [16] aim to detect out-of-distribution data by using machine learning techniques. In the following work are proposed two machine learning methodologies to be used for fast and reliable decision making between devices classified as OK and the others categories. The first methodology is based on population clustering by a statistical study of density with density-based spatial clustering of applications with noise (DBSCAN) [17], [18]. The second methodology is based on neural networks [19].

## II. IMPULSE RESPONSE-BASED METHOD

### A. WORKING PRINCIPLE

The measurement protocol consists of two antennas, one of which serves as a transmitting antenna, and the second is connected to an oscilloscope (see Fig. 1). The device under test is in close proximity to both antennas (about

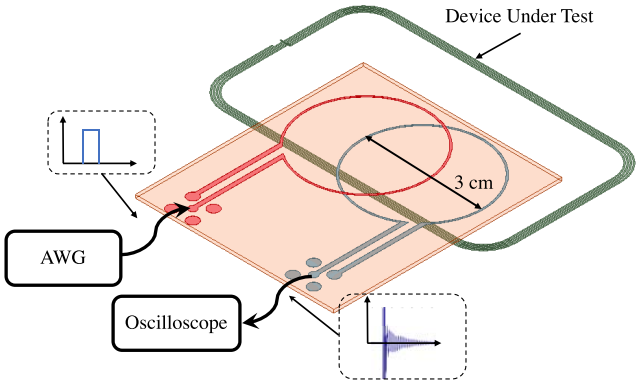


**FIGURE 1.** Working principle.

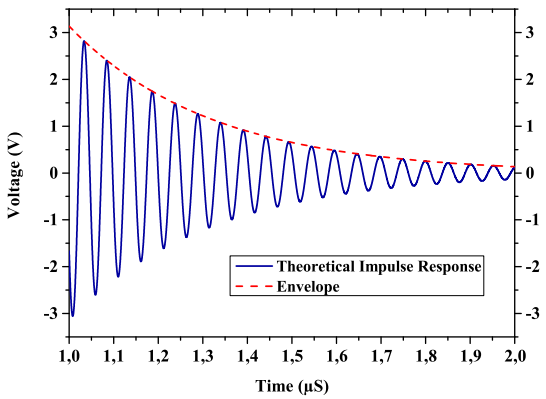


**FIGURE 2.** Ideal impulse response.

1 cm). A rectangular pulse with the characteristics shown in (1) is generated. The circuitry of an RFID tag can be modeled by a second-order resonant circuit of the RLC type (resistance, inductor, and capacitor). The response, $v(t)$, to a pulse $V_{\text{Pulse}}(t)$, is expressed as (2) [20]

$$V_{\text{Pulse}}(t) = \begin{cases} 0, & t \notin [t_{P\min}, t_{P\max}] \\ V, & t \in [t_{P\min}, t_{P\max}] \end{cases} \tag{1}$$

$$v(t) = \frac{K\omega_{\text{res}}}{\sqrt{1-\xi^2}} e^{-\xi\omega_{\text{res}}t} \sin\left(\omega_{\text{res}} t\sqrt{1-\xi^2}\right). \tag{2}$$

$K$ is a constant, and $\omega_{\text{res}}$ is the resonant frequency of the device. $\xi$ is the surge damping coefficient of the impulse response of the device. To avoid undesirable transient phenomena, acquisition begins 1 $\mu$s after the start of pulse generation. The theoretical output impulse response curve, $v(t)$, is shown in Fig. 2.

The response envelope can be expressed as [21]

$$e_{\text{nv}}(t) = \frac{K\omega_{\text{res}}}{\sqrt{1-\xi^2}} e^{-\xi\omega_{\text{res}}t}. \tag{3}$$

The period between two oscillations corresponds to the proper time. The expression of eigentime $T_{\text{p}}$ and the quality coefficient $Q$ is expressed in [21]

$$\text{With} \begin{cases} T_{\text{p}} = 1/(f_p) = \frac{2\pi}{\omega_{\text{res}}\sqrt{1-\xi^2}} \\ Q = \frac{1}{2\xi}. \end{cases} \tag{4}$$

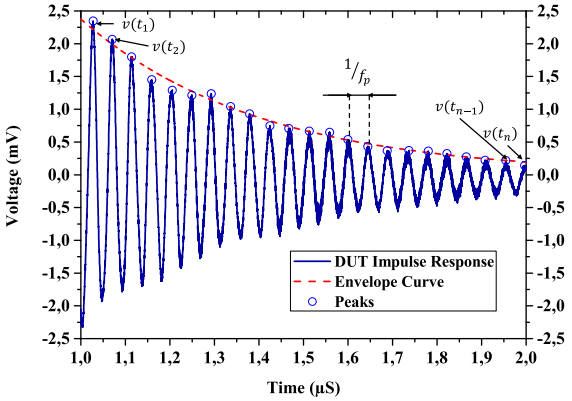


FIGURE 3. Impulse response (measure).

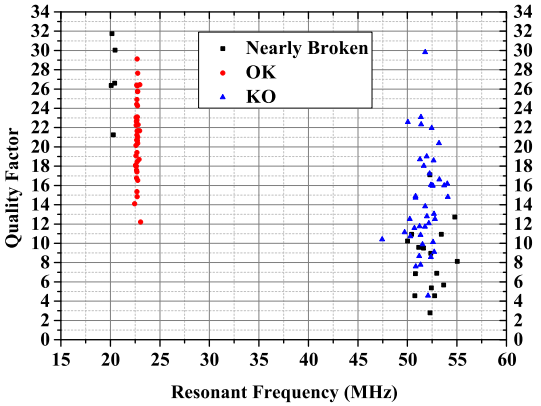


FIGURE 4. Impulse response measurement results.

### B. CURVE FIT METHOD IMPLEMENTATION

The impulse response of one of the DUT samples is shown in Fig. 3. It is possible to observe that the impulse response of the sample is not as ideal as the theoretical curve. To extract the resonant frequency and the quality factor, two approaches are proposed.

The first approach is based on the extraction of the envelope parameters of the impulse response. From (4), it is possible to describe the impulse response through an equation of type (5). The measurement environment must first fit this envelope which crosses through the local maximums of the impulse response by an equation of the form

$$e_{\mathrm{nv,fit}}(t) = \alpha e^{\beta t}. \tag{5}$$

The parameters (resonance frequency and quality factor) of the DUT are identified through the following equations:

$$\begin{cases} \beta = -\xi\omega_{\mathrm{res}} \\ f_p = \frac{\omega_{\mathrm{res}}\sqrt{1-\xi^2}}{2\pi} \end{cases} \tag{6}$$

$$\begin{cases} f_{\mathrm{res}} = \frac{\sqrt{(2\pi f_p)^2+\beta^2}}{2\pi} \\ Q = \frac{\sqrt{\omega_{\mathrm{res}}}}{2\beta}. \end{cases} \tag{7}$$

This method requires calculation and convergence capabilities on a given equation. If the working environment does not allow this type of calculation, the second method described in the next section allows to obtain the desired parameters.

### C. LOCAL MAXIMUMS METHOD IMPLEMENTATION

If the calculation capabilities of the analysis system are limited or do not allow the use of fit functions, it is possible to obtain the DUT parameters from the local maximums. The local maximum voltage can be expressed as follows:

$$v(t_x) = \mathrm{Ae}^{\frac{-\omega_{\mathrm{res}}t_x}{2Q}}. \tag{8}$$

From the voltage ratio between two local maximums (see (9)), it is possible to calculate the local quality factor by (10)

$$\frac{v(t_1)}{v(t_2)} = e^{\frac{-\omega_{\mathrm{res}}(t_2-t_1)}{2Q}} \tag{9}$$

$$\begin{cases} Q_{1,2} = \sqrt{\left(\frac{\pi}{\ln(\frac{v(t_1)}{v(t_2)})}\right)^2 + \frac{1}{4}} \\ f_{\mathrm{res}\,1,2} = \frac{t(2)-t(1)}{\sqrt{1-\frac{1}{4Q_{1,2}^2}}}. \end{cases} \tag{10}$$

The evolution of the envelope of the impulse response is nonlinear, as can be seen in Fig. 3.

The raw resonance frequencies and quality coefficient have been calculated from the local maximums $v(t_1)$ to $v(t_n)$. The quality coefficient and resonance frequency representative of the DUT were then deduced as the median value of the set of values obtained above

$$\begin{cases} Q = \mathrm{median}\left(Q_{1,2}, \ldots, Q_{n-1,n}\right) \\ f_{\mathrm{res}} = \mathrm{median}\left(f_{\mathrm{res}\,1,2}, \ldots, f_{\mathrm{res}\,n-1,n}\right) \end{cases}. \tag{11}$$

### D. RESULTS

The methodology based on local maximums has been applied to study the reliability of products during the personalization of electronic passports. During the manufacturing process of electronic passports, the chip is flashed to include the operating system, this operation is done by a contactless communication whose carrier is at 13.56 MHz.

The electronic passports are divided into three groups. The first group concerns the documents fully operational and without any anomaly, they are part of the OK group. The second group are devices that are not functional (broken antenna, chip HS, etc.), they are listed by the group KO. Finally, the last group concerns devices manufactured with a failure for which experience they show will no longer be operational well before the end of the life span desired by the application. These devices, classified as "Nearly Broken," are the most difficult to identify.

The results of the study presented in Fig. 4 show that the study of the resonance frequency alone is sufficient to discriminate the OK groups from the KO and "Nearly Broken." The dispersion of results concerning the quality coefficient is too large to reach the same conclusions.

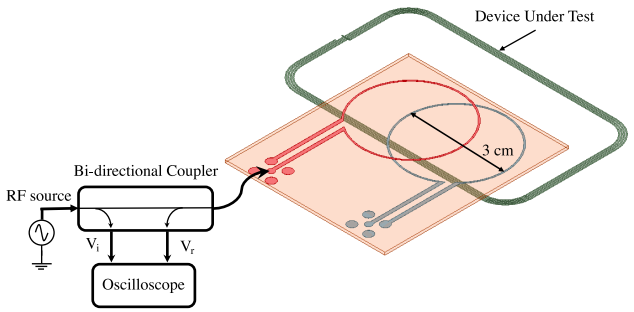


**FIGURE 5.** Operating principle.

In practice, even if this methodology presents promising results, however, it can be difficult to implement. Indeed, this method requires a specific generator (AWG or a pulse generator), but in production units, the sources used are generally sinusoidal sources centered around the carrier of the communication, i.e., 13.56 MHz. The generation of pulse can be damaging for the device under test, it generates a stress which can alter its operation and can generate disturbances on the adjacent production units.

Finally, the proposed method constitutes an additional step in the manufacturing process, which adds an incomparable amount of time to the passport personalization process. As a result, the productivity of the products is considerably reduced.

The method proposed in the following section is compatible with the constraints presented above.

## III. IMPEDANCE MEASUREMENT-BASED METHOD

### A. OPERATING PRINCIPLE

The method proposed in this section can be performed with the existing equipment of the production unit. It is based on the source which is used to personalize the document and to insert the OS of the device. The processing can be done in parallel with the personalization operation.

The measurement protocol requires only one antenna, which can be the one that is initially used to flash the component. In the implementation in this article, the antenna used is one of the antennas that was required for the method in the previous section.

The principle of the method proposed here is based on the methodology for extracting the *S*-parameters of a component. The impedance of the device is measured as the ratio between an incident wave transmitted by a 50-Ω internal impedance generator and a wave that has been reflected by the device under test and its environment. The isolation between the incident wave and the reflected wave is realized by a bidirectional coupler, as shown in Fig. 5. An oscilloscope with an internal impedance of 50 Ω is used to collect the data transmitted by the generator and reflected by the antenna.

The uniqueness of the implementation proposed here is that the measurement is carried out during the device customization phase, as exposed in [7]. As this personalization is carried out in a contactless way, there is a latency

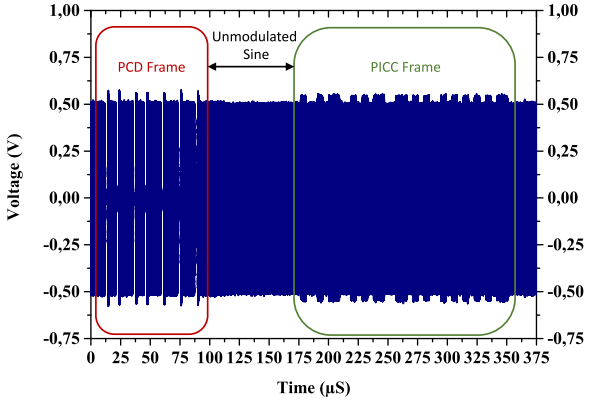


**FIGURE 6.** Communication between PCD and PICC (measure).

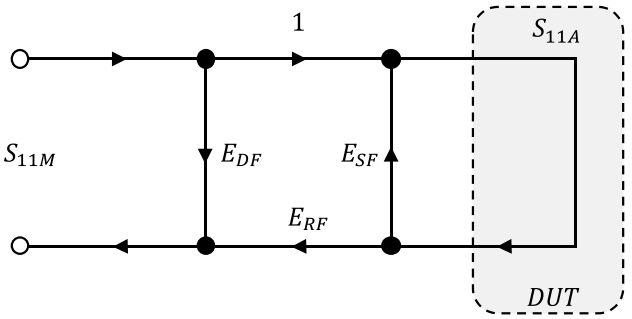


**FIGURE 7.** Flowgraph.

time between the end of the reader request, also called proximity coupling device (PCD), and the card responses called proximity integrate circuit card (PICC). During this latency phase, an unmodulated carrier is generated by the reader to power the device (see Fig. 6). Incident and reflected waves are picked up during this time by an oscilloscope and used as the basis for impedance measurement. The S11 acquired ($S_{11A}$) is the ratio between Vr (reflected wave) and Vi (incident wave).

The impedance measurement shown here can be a 1-port measurement which can be modeled as in Fig. 7. The difference between the measured *S*-parameter ($S_{11M}$) and the DUT *S*-parameter ($S_{11A}$) is related to different errors in the measurement environment. For 1-port measurements, the errors are limited to the effective directivity ($E_{DF}$), the effective source match error ($E_{SF}$), and the frequency response error ($E_{RF}$). These errors are related to source imperfections as well as to the measurement environment between the source and the DUT. In this study, the DUT will be represented by the PICC chip and the measurement environment will be the set of cables, coupler, and coupling between the PCD and PICC antennas.

The relationship between the DUT parameter S11 ($S_{11A}$) and the measured S11 parameter ($S_{11M}$) is presented in [22]

$$S_{11A} = \frac{S_{11M} - E_{DF}}{E_{RF} + (S_{11M} - E_{DF}).E_{SF}}. \quad (12)$$

To minimize errors, a calibration step is required. These calibrations are carried out by performing measurements in

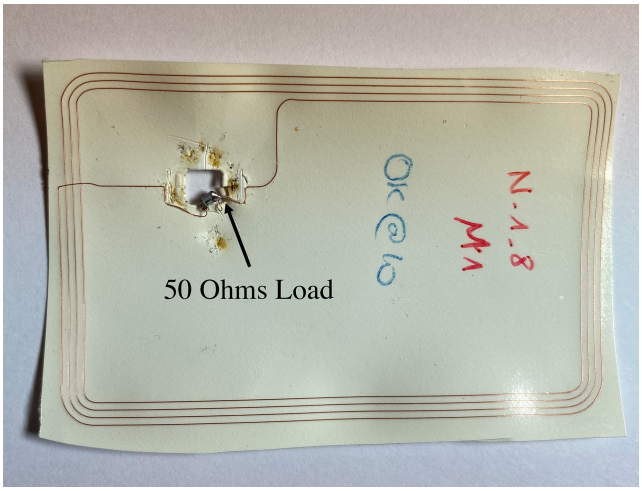


FIGURE 8. Antenna with load for calibration process.

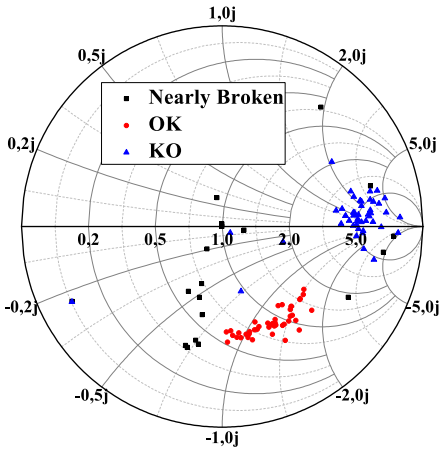


FIGURE 9. Impedance measurements method results.

the same faithful environment by substituting the DUT (here the chip) with known charges. The loads are short circuit, open circuit, and 50 Ω. In order to achieve these different loads, three antennas identical to those implemented in the PICCs (electronic passport) were made and then the chip was replaced by the required loads. The example of the antenna with a 50-Ω load is shown in Fig. 8.

The $S$ parameters of the different loads can be written according to the equations presented in [22]

$$\begin{cases} S_{11}^{\text{Open}} = E_{\text{DF}} + \frac{E_{\text{RF}}(1)}{1-E_{\text{SF}}(1)} \\ S_{11}^{\text{Short}} = E_{\text{DF}} + \frac{E_{\text{RF}}(-1)}{1-E_{\text{SF}}(-1)} \\ S_{11}^{\text{Load}} = E_{\text{DF}} + \frac{E_{\text{RF}}(0)}{1-E_{\text{SF}}(0)} \end{cases} \tag{13}$$

with $\Gamma_{\text{Open}} = 1$, $\Gamma_{\text{Short}} = -1$, and $\Gamma_{\text{Load}} = 0$. Errors can therefore be written as

$$\begin{cases} E_{\text{DF}} = S_{11}^{\text{Load}} \\ E_{\text{SF}} = \frac{S_{11}^{\text{Open}} + S_{11}^{\text{Short}} - 2E_{\text{DF}}}{S_{11}^{\text{Open}} - S_{11}^{\text{Short}}} \\ E_{\text{RF}} = -2\frac{\left(S_{11}^{\text{Open}} - E_{\text{DF}}\right)\left(S_{11}^{\text{Short}} - E_{\text{DF}}\right)}{S_{11}^{\text{Open}} - S_{11}^{\text{Short}}}. \end{cases} \tag{14}$$

The $S$ parameter of the DUT ($S_{11\text{A}}$), depending on the $S$ parameters of the calibration antennas, can therefore be expressed according to (15), shown at the bottom of the page [22].

The DUT impedance is calculated from (16) taking $Z_0$ as the normalization impedance, i.e., 50 Ω

$$Z_{11\text{A}} = \frac{1 + S_{11\text{A}}}{1 - S_{11\text{A}}} Z_0. \tag{16}$$

### B. RESULTS

The results of the experiment are presented in Fig. 9 in the form of a Smith chart. It can be seen that the devices identified as OK are grouped together in a certain area of the abacus and that the OK and NB devices are scattered throughout other areas of the abacus. The KO devices are mostly close to open circuit or high impedance and some closer to short circuit, this can be explained by a broken antenna, bad connection, or poor chip placement. It should be noted that there is sufficient clearance area between the OK and other devices to provide a criterion for rejecting undesired groups.

There are several explanations for the dispersion of the OK devices, the antennas in this article have been positioned manually with the highest possible accuracy, knowing that any error in position will result in measurement uncertainty. Despite these errors, the results obtained allow significant results in practice. The positioning of DUTs in a production environment will be much more reproducible.

Table 1 compares the two proposed measurement methods. Measurement methods are compared according to different criteria, and rated as "low" and "high" depending on their performance against these criteria. The impulse method is the most accurate for identifying ok devices and other populations. However, it suffers from major limitations: it requires the generation of pulse signals which are not within the capabilities of the production units and therefore require hardware adaptation, and the measurement has to be carried

$$S_{11\text{A}} = \frac{\left(S_{11\text{M}} - S_{11}^{\text{Load}}\right)\left(S_{11}^{\text{Open}} - S_{11}^{\text{Short}}\right)}{S_{11}^{\text{Load}} S_{11}^{\text{Short}} - 2S_{11}^{\text{Open}} S_{11}^{\text{Short}} + S_{11}^{\text{Open}} S_{11}^{\text{Load}} + S_{11\text{M}} S_{11}^{\text{Open}} + S_{11\text{M}} S_{11}^{\text{Short}} - 2S_{11\text{M}} S_{11}^{\text{Load}}}. \tag{15}$$

**TABLE 1. Compares the performance of the measurement methods (impulse and impedance).**

| Indicator | Impulse Response | Impedance Measurement |
|---|---|---|
| Ease of implementation | low | high |
| Accuracy | high | low |
| Processing Time | low | high |
| Limitations, Specificities | Hardware implementation Measurement constrainst | Verifications in manufacturing process |

out before or after customization, which considerably slows down the manufacturing process. Although less accurate, the second method has the dual advantage of not requiring a different source from the one required to customize the chip, and the analysis can be carried out during customization. It is also possible to interrupt the personalization process if a fault is detected on the device, which optimizes the process time.

## IV. AUTOMATED REJECTION BY MACHINE LEARNING

### A. INTRODUCTION

A next step in this study would be to obtain criteria to accept or reject automatically good and not good devices. Looking at the Smith chart, this one could be sliced in two zones, one containing the good devices, and the other containing all the other devices (bad or nearly broken).

But choosing the zones peremptorily could lead to a high sensitivity to different measurement conditions. This is why exploring algorithms that could learn where the two zones are, according to specific measurement conditions, could be much more robust than a "one size fits all" approach.

As one can clearly see different clusters of points on the Smith chart, the goal here is to detect these clusters automatically, or at least being able to draw two zones to separate good and not good devices. The automation is here significant, as the clusters may differ from one measurement system to another. These clusters or zones will be obtained from known samples and will be labeled as "master" clusters or zones. They could then be used as a basis for future comparisons in order to accept or reject devices. It would also be interesting to have criteria to automatically link a device to a master cluster or zone, or another one.

In our case, we can identify on the Smith chart three clusters and many outliers. A very well-known and often-used algorithm to cluster data is the *k*-means algorithms. But the main drawbacks of the basic algorithm are that it is sensitive to outliers, is not stable (the algorithms are initialized randomly, which can lead to sensitive differences for the result for two different executions of the algorithm), and also needs to know beforehand the number of clusters to find. Rather than trying to solve these problems one by one, we preferred to test the density-based scan, or DBSCAN algorithm, which is stable, finds by itself the number of possible clusters, and can deal with outliers. We also tested a neural network to try to achieve the same goal.

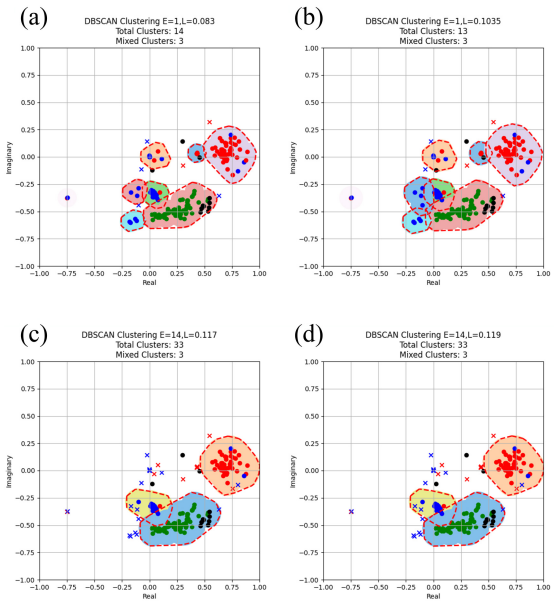


**FIGURE 10. DBSCAN clustering obtained from measured devices. Green points represent those identified as OK, red points are identified as KO, blue points are identified as "Nearly Broken," and black points are used for robustness study. (a) DBSCAN clustering *E*=1, *L*=0.083 (total clusters: 14; mixed clusters: 3). (b) DBSCAN clustering *E*=1, *L*=0.1035 (total clusters: 13; mixed clusters: 3). (c) DBSCAN clustering *E*=14, *L*=0.117 (total clusters: 33; mixed clusters: 3). (d) DBSCAN clustering *E*=14, *L*=0.119 (total clusters: 33; mixed clusters: 3).**

### B. STATISTICAL APPROACH

Using DBSCAN will require two parameters to feed the algorithm, the minimal size of the cluster, and a density parameter. These parameters have to be computed correctly in order to find relevant clusters, to which any new device will be assigned.

The algorithm proceeds as follows.

1) Select a range of realistic density parameters, according to the Smith chart.
2) Span this range of parameters.
3) For each of these parameters is applied the DBSCAN algorithm to create clusters.

This allows to select more precisely a range of density parameters that suits well our visual perception on the Smith chart, in order to find the best one: a density parameter that is at the same time selective enough to clearly draw the visually detected clusters, but not too selective to allow points that are at the limit of the current master clusters.

Fig. 10(a)–(d) displays the groupings of points relatively to different parameters. Each group has its own background color, and its convex hull is drawn. There are some isolated points that cannot be grouped with other points according to the parameters, and these points are detected automatically by the algorithm.

Doing so, we obtained the following results.

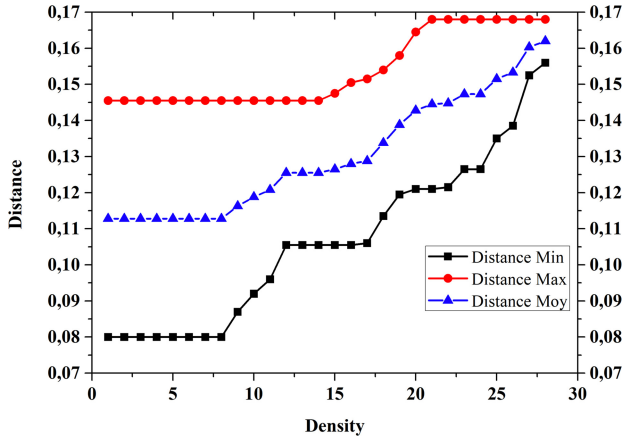


**FIGURE 11.** DBSCAN limit range.

1) On the Smith chart, the OK devices are usually well clustered.
2) The sparse nature of the nearly broken devices, and even the KO ones, make the task to cluster them difficult, but nevertheless they are easily identified as outliers, and so as "not OK" devices, which is enough for our purpose.
3) To test the robustness of the clustering, we will use a set of points that were not used during the clustering by DBSCAN.

Fig. 10(a) and (b) illustrates a grouping of points where the density required to perform the grouping is set to 1. The implication of this parameter is that clustering can be performed on small sets. However, it is not necessary in this study to identify all potential clusters, just to differentiate the OK points from the other. Consequently, to refine the grouping of points with exclusively OK status, the minimum density can be increased as shown in Fig. 10(c) and (d). By doing so, the groups in Fig. 10(a) and (b) that do not reach this minimum density will no longer be taken into account.

Fig. 10(b) and (d) also demonstrates that clustering (whatever density is used) can cover a larger area and, therefore, potentially group together a greater number of individuals, whether the detection distance is greater or smaller.

Based on the number of points available, we attempted to determine the detection limits for the group composed exclusively of OK status. For a density fluctuating between 1 and 28 individuals minimum, we obtained the results shown in Fig. 11. Minimum distances, shown in black, correspond to distances below which all OK statuses are not grouped together. The maximum distances, shown in red, are those beyond which statuses other than OK are grouped with OK statuses. It is not necessary to use a density greater than 28, because as the trend in the two curves shows, they seem to converge, making it impossible to group all OK statuses together at a density of 29.

The first observations obtained, presented in Fig. 11, allow us to postulate that the most suitable distance would be an average distance from the detection extremes of the group composed solely of OK statuses (illustrated in blue). However, the ideal density remains to be determined as it depends on the number of samples used to establish the grouping. The ideal density will be located before the convergence of the maximum and minimum limits of the detection distances.

In red dashed lines on Fig. 10, we have depicted an approximation of the zones identified by DBSCAN. These zones are established using a convex hull algorithm to encapsulate all the points and their detection zones used by DBSCAN. We can observe that using DBSCAN, with a grouping parameter between 1 and 14 points, allows at least one clustering distance that gathers all the OK points from the sample. This makes it possible to define an area exclusively composed of OK points without missing a single one. In each of these cases, we can see that the points used to assess robustness are located in the OK zone, unless they were measured in the presence of a metallic object. In that case, they will be too far from the OK zone.

The right choice of these parameters will enable the algorithm to be fed with a new point, coming from a device to test, and link it to one of the master clusters, or to consider it as an outlier. According to this, the device can then be considered OK or not.

### C. ARTIFICIAL NEURAL NETWORK APPROACH

An artificial neural network has also been trained to achieve the same goal. The neural net architecture has been made of three dense layers consisting of 50, 10, and 1 neurons, for a total of 671 trainable parameters. Both hidden layers were given the rectified linear unit (ReLU) activation function, while the output layer was equipped with the sigmoid.

The Smith chart, despite making the points closer together and leading to clusters being more apparent, exhibits a convoluted shape, leading to a complex internal model for the network. This is why it was preferred to apply this tool on the raw data, rather than on the data projected on the Smith chart.

The methodology used here has been to first normalize between 0 and 1 both coordinates of all data points by computing global min and max values on each axis. Then, the dataset has been split evenly (hence forming train and validation subsets), by taking care of having an even distribution of all three classes between the two parts. Additionally, the NB and KO classes were merged into a single not-OK class in each subset, therefore reducing the problem to a binary classification. Training on the first subset was then done for 150 epochs with the Adam optimizer. From these 150 epochs, the model with the lowest validation mean-squared error (MSE) loss has been kept.

A pitfall of this approach however was that the end result quality was highly dependent on the initial dataset split. To mitigate this 100 trainings were run, each with a different data split. The median model in terms of MSE loss computed on both the training and validation data has been selected.

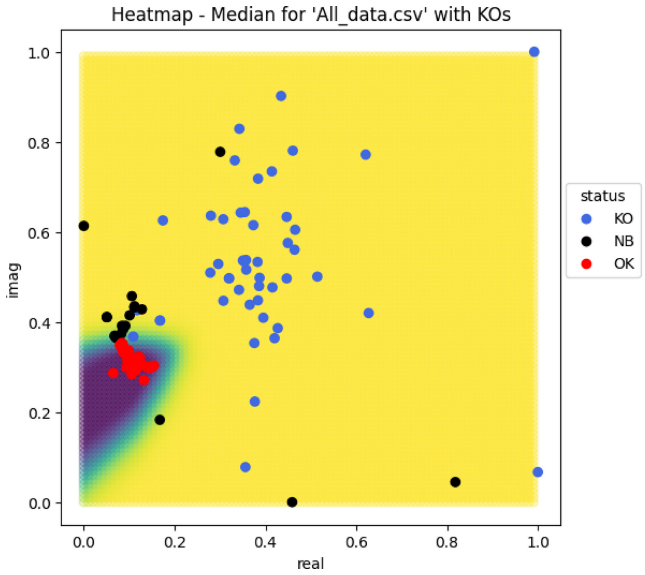


**FIGURE 12.** Heatmap for the median model on measured devices.

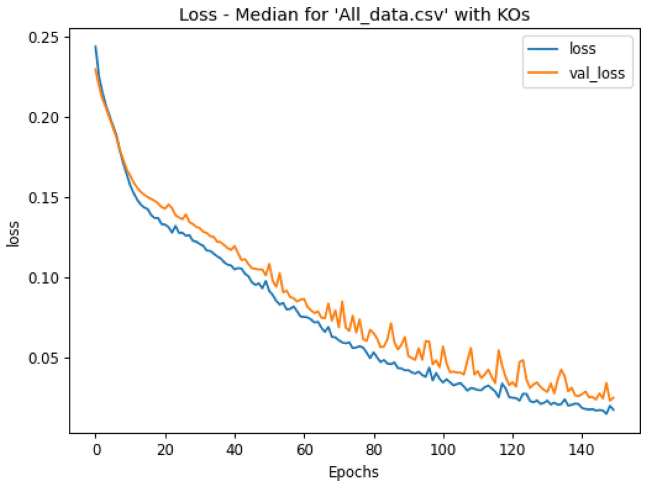


**FIGURE 13.** Training and validation loss curves.

The obtained results are as follows.

1) The median model achieves 100% accuracy on both the train and validation datasets.
2) In particular, the OK devices are clearly identified by the model.

Below are displayed two graphics showing characteristics of the trained neural network.

1) Fig. 12: A heatmap illustrating the classification capabilities of the model: dots in the blue area are assigned as OK, while dots in the yellow one are labeled as not-OK (keeping the color convention that red, blue, and black dots are OK, KO, and NB, respectively).
2) Fig. 13: The model train (blue) and validation (orange) MSE loss curves during training.

The average inference time for a single sample is around 60 ms on a mid-range CPU, allowing this method to be done in real time during the passport personalization process.

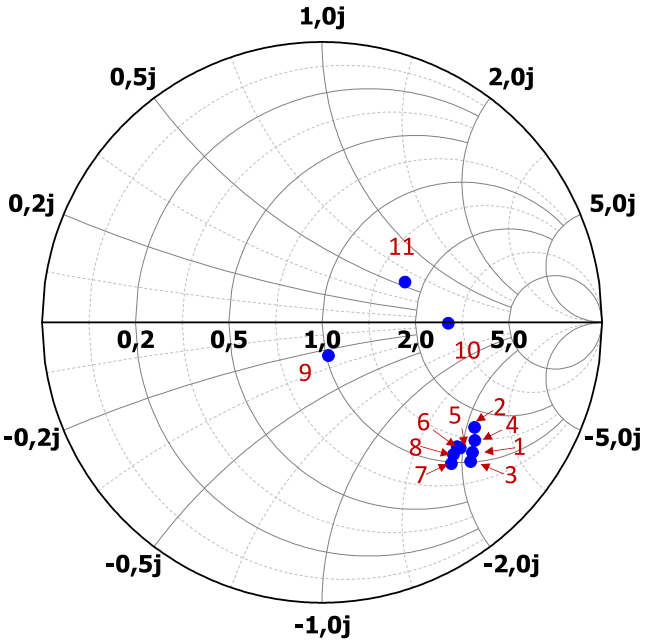


**FIGURE 14.** Smith chart representation of robustness study.

However, some work has been done to lower further said inference time by saving the heatmap image underlying array, in order to directly read a precomputed approximation of the activation value of a given sample from the heatmap. The image has been sampled in a $100 \times 100$ resolution, and its values are quantized on 8-bit to reduce its size. This induces a small loss in fidelity from the neural network outputs (less than 1% of total loss relative difference) while retaining 100% accuracy on the whole dataset, in exchange for quicker response times: 20 $\mu$s per sample on average.

The source code for the artificial neural network method is available at [23].

### D. ROBUSTNESS STUDY

Another validation step has been done in order to confirm the effectiveness and robustness of the two previous methods, by testing them on a new dataset containing OK, KO, NB, and ROB samples in Fig. 14. ROB points are measurements of the same OK device which have been made deliberately noisy (see Table 2 for more details). From an operational point of view, this involves studying the impact of device positioning errors (placement, angle of the device, presence of metal plates, etc.).

Additionally, the normalization parameters used in the neural network approach have been computed on the previous dataset and are not to be recomputed. The new validation step will serve to show that the normalization generalizes well to new data points (from new measured devices).

The new validation dataset without the ROB points yields once again 100% accuracy with the neural network method, as well as with the precomputed heatmap approach. However, the ROB points which are associated with the presence of a

**TABLE 2.** Robustness study parameters.

| Indicator | Deviation |
|---|---|
| 1 | Initial product |
| 2 | +1cm x |
| 3 | +1cm y |
| 4 | 45° |
| 5 | 90° |
| 6 | -90° |
| 7 | -1cm x |
| 8 | -1cm y |
| 9 | metal at 1cm |
| 10 | metal at 2cm |
| 11 | metal at 3cm |

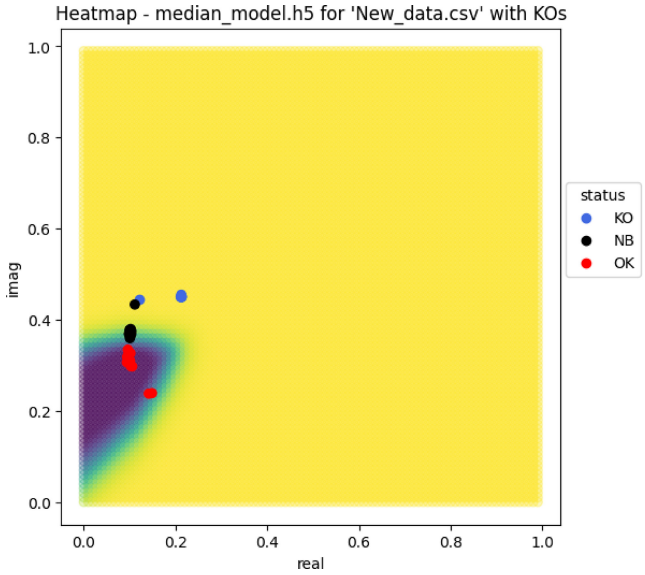


**FIGURE 15.** Heatmap for the new data.

metal plate are not classified properly as OK samples, but the other ROB points are classified correctly, except for the device N°2. See Fig. 15 for a heatmap drawn with the new dataset.

### *E. RESULTS*

The proposed methods demonstrate the efficiency of an automated rejection system using machine learning techniques, the resulting systems achieving perfect accuracy scores on both datasets, and being robust to noise added to the data. Furthermore, these methods are fast enough to be integrated into the manufacturing process of the devices. Table 3 summarizes some characteristics of the suggested approaches.

The robustness study indicates that the measurement process is very sensitive to metallic elements which are not taken into account during calibration. It is also sensitive to misalignment of more than 1 cm from the center point. It is, however, tolerant of an angle that could be introduced when placing these devices. This study gives the boundary conditions for the use of this method. It should be noted that such deviations are not tolerated in a controlled manufacturing environment.

**TABLE 3.** Compares the AI methods used.

| Indicator | Statistical Approach | Artificial Neural Network Approach | Precomputed heatmap |
|---|---|---|---|
| Ease of implementation | ++ | ++ | ++ |
| Accuracy | 100% | 100% | 100% |
| Processing Time | | 60 ms | 20 $\mu$s |

## V. CONCLUSION

This article presents several methodologies for contactless devices characterization. Each of these methods has its own characteristics, strengths, and weaknesses.

The first method requires two distinct antennas, one dedicated to transmission and the other to listening to the response. The impulse method makes it possible to distinguish OK devices from KO and NB devices through the study of the resonance frequency alone. However, it is necessary to use an additional impulse source that is not part of the initial contactless device customization device. This method lengthens the customization process and can cause electromagnetic compatibility (EMC) issues.

The second methodology can be inserted into the flow of contactless device customization. OK devices from other product categories. It requires a calibration step that can be carried out at the very beginning of the process.
This method can be done in parallel with the customization steps, which does not add time to the manufacturing process of the devices. The elements necessary to perform the operations can easily be added to a manufacturing environment. These two facts can be differentiated in a context where production delay is crucial.

With these two methods, it is possible to distinguish devices that may have a premature life span and thus increase the quality of the production flow as a whole.

Two machine learning methods have been studied and both have produced convincing results. Their execution speed is suitable for integration into the personalization process. The robustness study highlighted the requirement for significant reproducibility in the positioning of devices.

## VI. PERSPECTIVES

There are several prospects for the proposed work. A population discretization method can focus on the transient parameters of communications (rise time, fall time, overshoot, etc.). Design faults will inevitably have an impact on these parameters.

As the proposed machine learning methods show excellent accuracy scores on the given data, and since inference times are low enough for the proposed methodology to work in real time (especially using the heatmap solution), the following points are proposed to improve the exposed work.

1) Increase the size of both the training and validation datasets, with the goal of reducing any uncertainty on the claimed accuracy scores.
2) Realize more thorough robustness tests, in order to determine which level of measurement noise can be acceptable for our systems to still work correctly.
3) In the prospect that our solutions do not perform well enough on more (potentially noisy) data, several other machine learning techniques could be tested, for example, hierarchical clustering or decision trees.

## REFERENCES


[1] *EMV® Contactless Specifications for Payment Systems Book D EMV Contactless*, EMVCo, Foster City, CA, USA, Mar. 2016.
[2] *Identification Cards-Contactless Integrated Circuit(s) Cards—Proximity Cards*, ISO Standard 14443, Apr. 2018.
[3] *Identification Cards Contactless Integrated Circuit Cards Vicinity Cards Part 1: Physical Characteristics*, ISO Standard 15693, Oct. 2010.
[4] *NFC Forum Technical Specification: Analog Technical Specification (Version 2.1)*, NFC Forum, Hyderabad, India, 2017.
[5] *Identification Cards—Test Methods*, ISO Standard 10373, Sep. 2018.
[6] *Identification Cards Test Methods Part 7: Vicinity Cards*, ISO Standard 10373, May 2005.
[7] B. Couraud, T. Deleruyelle, E. Kussener, and R. Vauché, "Real-time impedance characterization method for RFID-type backscatter communication devices," *IEEE Trans. Instrum. Meas.*, vol. 67, no. 2, pp. 288–295, Nov. 2018.
[8] J. Grosinger, B. J. Deutschmann, L. Zoscher, M. Gadringer, and F. Amtmann, "HF RFID tag chip impedance measurements," *IEEE Trans. Instrum. Meas.*, vol. 71, pp. 1–11, 2022.
[9] S. L. Chen, K. H. Lin, and R. Mittra, "A measurement technique for verifying the match condition of assembled RFID tags," *IEEE Trans. Instrum. Meas.*, vol. 59, no. 8, pp. 2123–2133, Aug. 2010.
[10] M. Gebhart, "Analytical considerations for an ISO/IEC14443 compliant SmartCard transponder," in *Proc. 11th Int. Conf. Telecommun., ConTEL*, 2011, pp. 9–16..
[11] L. Mats, J. T. Cain, and M. H. Mickle, "An indirect non-invasive method for measuring input impedance and connection effects of an RFID tag antenna," in *Proc. 68th ARFTG Conf. Meas. Emerg. Technol.,* 2006, pp. 1–7.
[12] L. Mats, J. T. Cain, and M. H. Mickle, "The in-situ technique for measuring input impedance and connection effects of RFID tag antenna," *IEEE Trans. Autom. Sci. Eng.*, vol. 6, no 1, pp. 4–8, Jan. 2009.
[13] D. Ulmer and G. Ciná, "Know your limits: Uncertainty estimation with ReLU classifiers fails at reliable OOD detection," in *Proc. Conf. Uncertainty Artif. Intell.*, 2020, pp. 1–11. [Online]. Available: https://api.semanticscholar.org/CorpusID:235390924
[14] D. Ulmer and G. Ciná, "Know your limits: Uncertainty estimation with ReLU classifiers fails at reliable OOD detection (supplementary material)," 2021. [Online]. Available: https://api.semanticscholar.org/CorpusID:261231352
[15] M. Markou and S. Singh, "Novelty detection: A review—Part 1: Statistical approaches," *Signal Process.*, vol. 83, no. 12, pp. 2481–2497, 2003. [Online]. Available: https://api.semanticscholar.org/CorpusID:17490415
[16] L. Perini, V. Vercruyssen, and J. Davis, "Quantifying the confidence of anomaly detectors in their example-wise predictions," in *Proc. ECML/PKDD*, 2020, pp. 227–243. [Online]. Available: https://api.semanticscholar.org/CorpusID:232082434
[17] D. Deng, "DBSCAN clustering algorithm based on density," in *Proc. 7th Int. Forum Electr. Eng. Autom., (IFEEA)*, 2020, pp. 949–953.
[18] M. Celik, F. Dadaser-Celik, and A. S. Dokuz, "Anomaly detection in temperature data using DBSCAN algorithm," in *Proc. INISTA Int. Symp. Innovat. Intell. Syst. Appl.*, 2011, pp. 91–95.
[19] Y. A. LeCun, L. Bottou, G. B. Orr, and K.-R. Müller, "Efficient BackProp" in *Neural Networks: Tricks of the Trade*. Berlin, Germany: Springer, 2012, pp. 9–48. [Online]. Available: https://doi.org/10.1007/978-3-642-35289-8_3
[20] J. D. Irwin and R. M. Nelms, *Basic Engineering Circuit Analysis*, 11th ed. Hoboken, NJ, USA: Wiley, 2011.
[21] N. S. Nise, *Control Systems Engineering*, 7th ed. Hoboken, NJ, USA: Wiley, 2019.
[22] J. P. Dunsmore, *Handbook of Microwave Component Measurements: With Advanced VNA Techniques*, 2nd ed. Hoboken, NJ, USA: Wiley, 2012.
[23] F. Sananes. "The source code for the neural net classification is available." [Online]. Available: https://github.com/Carath/AI-Assistance-for-Diagnostic-Measurement


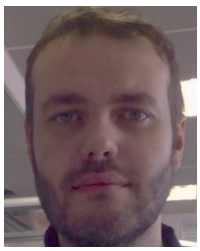

**THIBAUT DELERUYELLE** (Member, IEEE) received the engineering degree in electronics from the Polytechnical Engineering School, Polytech'Lille, Villeneuve-d'Ascq, France, in 2006, and the Ph.D. degree in micro and nanoelectronics from the University of Aix-Marseille, Marseille, France, in 2010.

In 2010, he integrates the Engineering School ISEN Mediterranée (Superior Institute of Electronic and Digital), Toulon, France, as a Research Lecturer, where he has been the Co-Director of research and development activities since 2022. Since 2010, he has been an Associate Researcher with the IM2NP RFID OC Team (UMR CNRS 7334), Toulon. His research focuses on integrated antennas, embedded systems, NFC, and IoT applications.

**AMAURY AUGUSTE** graduated from ISEN Engineering School, Toulon, France, in 2016. He received the Ph.D. degree in image processing and data analysis from the Université de Bretagne Occidentale, Brest, France, in 2022.

Since 2016, he has been a Teacher-Researcher with the ISEN Méditerranée Engineering School (Institut Supérieur de l'Electronique et du Numérique), Toulon, with research interests in image analysis, data analysis, and artificial intelligence.

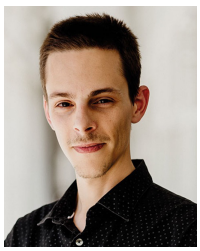

**FLORIAN SANANES** received the master's degree in mathematics from Aix-Marseille University, Marseille, France, in 2014, and the engineering degree from ISEN Mediterranee School, Toulon, France, in 2021.

In 2022, he integrated ISEN as a Research Lecturer. His research focuses on applied artificial intelligence technologies.

**GHISLAIN OUDINET** received the degree in applied engineering from ISEN, Toulon, France, in 1998, and the Ph.D. degree from Université Jean Monnet, Saint-Étienne, France, in 2003.

His Ph.D. focused on the characterization of nuclear fuels by image analysis, and on methods and algorithms to obtain trusted indicators to characterize different microstructures. After working with the Nuclear Research Center, Cadarache, Saint-Paul-lez-Durance, France, he joined the Pedagogical Team, Yncréa Méditerranée, Toulon, in 2004 as a Research Lecturer. He has been involved in many software research and development projects, notably where signal treatment algorithms have to be adapted to achieve the best possible performance.